東北大学機関リポジトリ
TOUR
Tohoku University Repository

A NuSTAR and XMM-Newton Study of the Two Most Actively Star-forming Green Pea Galaxies (SDSS J0749+3337 and SDSS J0822+2241)

A *NuSTAR* and *XMM-Newton* Study of the Two Most Actively Star-forming Green Pea Galaxies (SDSS J0749+3337 and SDSS J0822+2241)

Taiki Kawamuro[1,7] , Yoshihiro Ueda[2] , Kohei Ichikawa[3,4] , Masatoshi Imanishi[1] , Takuma Izumi[1,8] ,
Atsushi Tanimoto[2,7] , and Kenta Matsuoka[5,6,7]

[1] National Astronomical Observatory of Japan, Osawa, Mitaka, Tokyo 181-8588, Japan; taiki.kawamuro@nao.ac.jp
[2] Department of Astronomy, Kyoto University, Kitashirakawa-Oiwake-cho, Sakyo-ku, Kyoto 606-8502, Japan
[3] Frontier Research Institute for Interdisciplinary Sciences, Tohoku University, Sendai 980-8578, Japan
[4] Astronomical Institute, Tohoku University, Aramaki, Aoba-ku, Sendai, Miyagi 980-8578, Japan
[5] Dipartimento di Fisica e Astronomia, Universitá degli Studi di Firenze, Via G. Sansone 1, I-50019 Sesto Fiorentino, Italy
[6] INAF Osservatorio Astrofisico di Arcetri, Largo Enrico Fermi 5, I-50125 Firenze, Italy

Abstract

We explore X-ray evidence for the presence of active galactic nuclei (AGNs) in the two most actively star-forming Green Pea galaxies (GPs), SDSS J0749+3337 and SDSS J0822+2241, which have star formation rates (SFRs) of 123 $M_\odot$ yr^{-1} and 78 $M_\odot$ yr^{-1}, respectively. The GPs have red mid-infrared (MIR) spectral energy distributions and higher 22 μm luminosities than expected from a proxy of the SFR (Hα luminosity), consistent with hosting AGNs with 2–10 keV luminosities of $\sim 10^{44}$ erg s^{-1}. We thus obtain and analyze the first hard (>10 keV) X-ray data observed with *NuSTAR* and archival *XMM-Newton* data below 10 keV. From the *NuSTAR* ≈ 20 ks data, however, we find no significant hard X-ray emission. By contrast, soft X-ray emission with 0.5–8 keV luminosities of $\approx 10^{42}$ erg s^{-1} is significantly detected in both targets, which can be explained only by star formation (SF). A possible reason for the lack of clear evidence is that a putative AGN torus absorbs most of the X-ray emission. Applying a smooth-density AGN torus model, we determine minimum hydrogen column densities along the equatorial plane ($N_{\rm H}^{\rm eq}$) consistent with the nondetection. The results indicate $N_{\rm H}^{\rm eq} \gtrsim 2 \times 10^{24}$ cm^{-2} for SDSS J0749+3337 and $N_{\rm H}^{\rm eq} \gtrsim 5 \times 10^{24}$ cm^{-2} for SDSS J0822+2241. Therefore, the GPs may host such heavily obscured AGNs. Otherwise, no AGN exists and the MIR emission is ascribed to SF. Active SF in low-mass galaxies is indeed suggested to reproduce red MIR colors. This would imply that diagnostics based on MIR photometry data alone may misidentify such galaxies as AGNs.

Key words: galaxies: active – galaxies: individual (SDSS J074936.77+333716.3 and SDSS J082247.66 +224144.0) – infrared: galaxies – X-rays: galaxies

1. Introduction

There now seems to be a general consensus that supermassive black holes (SMBHs) with masses above a million solar masses ($M_\odot$; Kormendy & Richstone 1995; Kormendy & Ho 2013) are ubiquitous in the center of massive galaxies. The growth history of SMBHs can be traced based on the luminosity functions of active galactic nuclei (AGNs; e.g., Ueda et al. 2003, 2014; Shankar et al. 2004; Hasinger et al. 2005), and the results suggest that mass accretion is a dominant mechanism. This further infers the existence of massive black holes (mBHs) with masses in the range of $\sim 10^{3-6}$ $M_\odot$ (Marconi et al. 2004). Given the correlation between the central SMBH mass and stellar properties of the galaxy bulge (Magorrian et al. 1998; Gebhardt et al. 2000; Marconi & Hunt 2003; Gültekin et al. 2009), mBHs are predicted to reside in low-mass galaxies and, indeed, have been found observationally (Thornton et al. 2008; Baldassare et al. 2015; Nguyen et al. 2017, 2018).

Some theoretical studies, however, have argued that not all low-mass galaxies host mBHs (Volonteri et al. 2008; Volonteri 2010) and that it depends on seed formation mechanisms such as a remnant of massive Population III stars (Bromm & Yoshida 2011), the end-product of very massive stars formed through stellar mergers in dense star clusters (e.g., Gürkan et al. 2004), and the result of the direct collapse of primordial dense

gas (Haehnelt & Rees 1993; Begelman et al. 2006; Lodato & Natarajan 2006). In other words, the mBH occupation fraction, as well as the mBH mass function in local low-mass galaxies, are expected to provide insights into how the seeds of SMBHs formed. Thus, mBH fractions have been enthusiastically measured under the assumption that the observed fractions of AGNs should be independent of the galaxy mass. (Greene 2012; Mezcua et al. 2016, 2018; Reines & Comastri 2016). So far, fractions constrained using soft X-ray observations (e.g., Greene 2012) support the view that direct collapse is a dominant process, where a lower occupation fraction is expected. Given that heavily obscured AGNs may be missed, however, a higher fraction is possible and may indeed favor the other scenarios. Thus, in order to draw a robust conclusion, it is necessary to construct as unbiased a sample as possible.

X-ray surveys are very important for sample construction (e.g., Chen et al. 2017). As described above, the soft X-ray (<10 keV) band has often been used for such studies but is easily biased against obscured systems. Moreover, given a theoretical prediction of increased soft X-ray luminosity in young and low-metallicity galaxies (e.g., Linden et al. 2010; Fragos et al. 2013) and subsequent soft X-ray observations that have confirmed this (Basu-Zych et al. 2013; Brorby et al. 2016; Brorby & Kaaret 2017), it is possible to misidentify star formation-induced soft X-ray emission as that from an AGN. By contrast, the hard X-ray (>10 keV) band overcomes the above difficulties due to its high penetrating power and reduced

---

[7] JSPS fellow.
[8] NAOJ fellow.

Table 1
Information Relating to Two Green Pea Galaxies

SDSS Name	R.A. (J2000) (degrees)	Decl. (J2000) (degrees)	z	D_L (Gpc)	SFR ($M_\odot$ yr^{-1})	$\log(M_\star/M_\odot)$	$\log(\mathrm{sSFR/Gyr}^{-1})$	$12 + \log(\mathrm{O/H})$	$L_{\mathrm{H}\alpha}$ (10^{42} erg s^{-1})
(1)	(2)	(3)	(4)	(5)	(6)	(7)	(8)	(9)	(10)
J0749+3337	117.403215	33.621219	0.2733	1.40	123 ± 51	9.49	1.11 ± 0.02	8.29	7.4 ± 0.3
J0822+2241	125.698590	22.695578	0.2163	1.07	78 ± 34	8.43	1.98 ± 0.05	8.08	4.7 ± 0.5

Note. (1) SDSS source name. (2) R.A. (3) decl. (4) Redshift. (5) Luminosity distance. (6) SFR that takes account of the dust-obscured and unobscured SFRs (see Section 5.1 for derivation). (7) Stellar mass from Izotov et al. (2011). (8) sSFR derived by following Hainline et al. (2016), where SFRs were calculated with the Hα luminosity as $\log(\mathrm{SFR}/M_\odot \, \mathrm{yr}^{-1}) = \log(L_{\mathrm{H}\alpha}/\mathrm{erg \, s}^{-1}) - 41.27$. (9) Oxygen abundance ratio from Izotov et al. (2011). (10) Extinction-corrected Hα luminosity taken from Cardamone et al. (2009).

contamination by stellar light. Mid-infrared (MIR) color–color selection is another option that is unbiased against absorption; it relies on characteristic MIR colors produced by AGN-heated hot dust (Jarrett et al. 2011; Stern et al. 2012; Mateos et al. 2012) and has been examined for various samples (e.g., Gandhi et al. 2015; Kawamuro et al. 2016b; Ichikawa et al. 2017). Some studies applied *Wide-field Infrared Survey Explorer* (*WISE*) AGN diagnostics to low-mass galaxies and created large AGN candidate samples (Satyapal et al. 2014; Sartori et al. 2015; Secrest et al. 2015). However, Hainline et al. (2016) demonstrated that star-forming low-mass galaxies, particularly those with very young stellar populations and high specific star formation rates (sSFRs), could produce MIR colors similar to those of *WISE*-selected AGN. Thus, hard X-ray data are important and need to be investigated.

In this paper, we discuss the presence of AGNs in two low-mass galaxies ($M_\star \sim 10^9 \, M_\odot$) SDSS J074936.77+333716.3 and SDSS J082247.66+224144.0 (hereafter, J0749+3337 and J0822+2241), i.e., the two highest star formation rate (SFR) Green Pea galaxies (GPs). As explained below, they are optically classified as non-AGN hosts, but their MIR properties are consistent with having AGNs. Their basic properties can be found in Table 1.

Through the Galaxy Zoo project (Lintott et al. 2008), GPs were first identified in the local universe ($0.1 < z < 0.4$) by their green, unresolved (i.e., $\lesssim 1''$) compact morphology in Sloan Digital Sky Survey (SDSS) images (Cardamone et al. 2009). These features were interpreted as [O III]$\lambda5007$ emission with high equivalent widths (EWs; ≈ 700 Å on average) within ≈ 5 kpc. Figure 13 of Cardamone et al. (2009) demonstrated that the EWs are generally higher than those observed in galaxies with similar redshifts and g-band magnitudes. Note that the EWs of J0749+3337 and J0822+2241 are ≈ 340 Å and ≈ 1040 Å, respectively. Cardamone et al. (2009) reported that among 112 GPs with good quality optical spectra, nine GPs show broad Balmer lines, and thus were classified as AGN hosts. They applied the optical Baldwin–Phillips–Terlevich diagram (Kewley et al. 2001; Kauffmann et al. 2003) to the remaining 103 sources, and the result was that 23 GPs are classified as AGNs while 80 GPs, including our two targets, are classified as star-forming galaxies.

The star-forming GPs have low-stellar masses ($10^{8.5}$–$10^{10} \, M_\odot$) and resemble high-redshift galaxies in terms of size, morphology, large emission lines, reddening, luminous UV emission (i.e., high SFRs), and low metallicity (Cardamone et al. 2009; Izotov et al. 2011). Thus, the GP sample is suggested to offer a valuable opportunity to investigate an early phase of galaxy growth in detail. Many interesting results, such as star-forming conditions and the escape fraction of ionizing radiation, have been reported, to date (e.g., Chakraborti et al. 2012; Jaskot & Oey 2013; Henry et al. 2015). However, few studies have mentioned the presence of

Table 2
X-Ray Data List

SDSS Name	Observatory	ObsID	Obs. Date (UT)	Exp. (ks)
(1)	(2)	(3)	(4)	(5)
J0749+3337	*XMM-Newton*	0690470101	2013 Mar 25	20/22
	NuSTAR	60301008002	2018 Mar 23	34
J0822+2241	*XMM-Newton*	0690470201	2013 Apr 06	28/33
	NuSTAR	60301009002	2018 Feb 04	44

Note. Columns: (1) SDSS source name. (2) Observatory name. (3) Observation ID. (4) Observation start date. (5) Exposure after data reduction. For the *XMM-Newton* observations, the PN and MOS 1 plus 2 exposure times are denoted separately, while the FPMA and FPMB merged exposures are represented in the *NuSTAR* rows.

AGNs by utilizing the MIR or soft X-ray observational data (Yang et al. 2016; Svoboda et al. 2018).

With regard to our GPs, no AGN sign was found from optical spectra. As suggested above, the GPs have inactive galaxy-like [O III]$\lambda5007$/Hβ and [N II]$\lambda6583$/Hα flux ratios.[9] Also, their extinction-corrected [O III] luminosity ($\approx 10^{43}$ erg s^{-1}) to X-ray (2–10 keV) luminosity ratios, where the X-ray luminosities are estimated from the MIR emission (see Section 2), are slightly higher (≈ 0.05) than the average of a nearby AGN sample of Ueda et al. (2015; ~ 0.03). The extinction correction is made by following Ueda et al. (2015). Thus, their [O III] emission may be dominated by SF, consistent with the above. However, their MIR properties are consistent with those observed for AGN hosts (see Section 2). This apparent discrepancy could be explained if a mass accretion black hole is deeply buried in the surrounding material, and therefore the narrow-line region remains absent (e.g., Imanishi et al. 2001, 2006, 2008, 2010; Ueda et al. 2007; Ichikawa et al. 2014). To provide new insights into this discussion, we present the first hard X-ray data obtained with *NuSTAR* (Harrison et al. 2013), currently the most sensitive hard X-ray (3–80 keV) observatory. Additionally, soft X-ray properties are examined using *XMM-Newton* (Jansen et al. 2001) archival data. The *NuSTAR* and *XMM-Newton* observations were conducted in 2018 (PI: Kawamuro) and in 2013 (PI: Ehle), respectively, and the log of these X-ray observations is given in Table 2.

---

[9] We note that J0822+2241 may have moderately high [O III]$\lambda5007$/Hβ and [N II]$\lambda6583$/Hα flux ratios of 0.75 and -1.0 in logarithmic scale, as calculated from the spectral line properties provided by the SDSS DR7 site of http://skyserver.sdss.org/dr7/en/tools/search/radial.asp. Thus, it may be classified as an AGN host, but in this paper we follow the results from a spectral analysis by Cardamone et al. (2009). On the other hand, the spectral lines of J0749+3337 from the site are still consistent with an inactive galaxy.
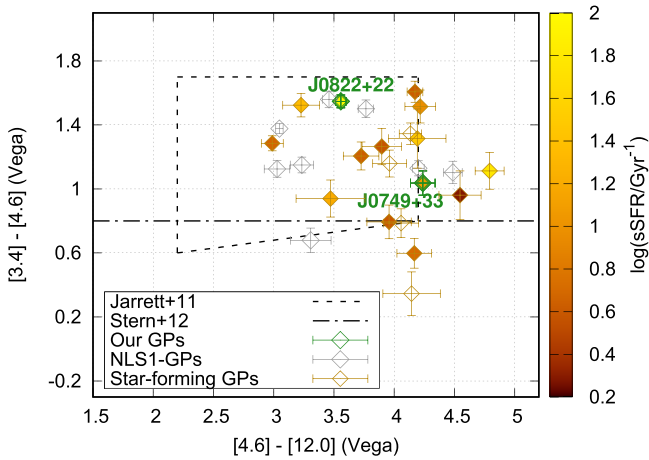
Figure 1. MIR 4.6–12.0 μm vs. 3.4–4.6 μm color–color plot. Black dashed and dotted–dashed lines represent the AGN selection criteria proposed by Jarrett et al. (2011) and Stern et al. (2012), respectively. Only those whose stellar masses were constrained by Izotov et al. (2011) are color-coded according to the right-hand color bar for the sSFR. Four star-forming GPs are located outside the figure and are generally in the upper right direction.

The remainder of this paper is organized as follows. First, we briefly summarize the MIR properties of J0749+3337 and J0822+2241 based on the *WISE* data in Section 2. In Section 3, we present an analysis of the *NuSTAR* data, and report the nondetection of the GPs in the hard X-ray band. In Section 4, we perform spectral analysis of the *XMM-Newton* data. A discussion and summary are given in Sections 5 and 6, respectively. Throughout this paper, we assume a ΛCDM cosmology with $H_0 = 70\,\mathrm{km\,s^{-1}\,Mpc^{-1}}$, $\Omega_m = 0.3$, and $\Omega_\Lambda = 0.7$. We utilize HEASoft version 6.22 for X-ray data reduction, and XSPEC version 12.9.1p (Arnaud 1996) for spectral analysis. The solar abundance table provided in Wilms et al. (2000), where the oxygen abundance ratio of $12 + \log(\mathrm{O/H})$ is 8.69, is adopted. Errors attached to X-ray spectral parameters are given at 90% confidence limits for a single parameter of interest by following convention, while others are quoted at the 1σ confidence level unless otherwise stated.

2. *WISE* MIR Properties

We present that in the MIR (3–22 μm) band the GPs have red colors, steep spectral indices, and luminous emission, consistent with the presence of an AGN. Their MIR data were taken from the AllWISE data release, which combined the data taken from the four-band cryogenic phase (Wright et al. 2010) and the NEOWISE post-cryo phase (Mainzer et al. 2011). The GPs were detected in all four bands (*W1*: 3.4 μm, *W2*: 4.6 μm, *W3*: 12 μm, and *W4*: 22 μm) with signal-to-noise ratio (S/N) above 12 (i.e., `ph_qual = A`) and little saturation (i.e., `w[1,2,3,4]sat ≈ 0`). The photometry flag of `ccflag = 0` guaranteed that our sources were unaffected by known artifacts (e.g., contamination and/or biased flux due to proximity to an image artifact). The observed magnitudes were converted into flux densities by assuming a spectral index of $\alpha = 2$ in the form of $S_\nu \propto \nu^{-\alpha}$, close to those obtained by our spectral energy distribution (SED) fits (see below).

Figure 1 shows a *WISE* color–color plot of the GPs together with two AGN selection regions proposed by Stern et al. (2012)

and Jarrett et al. (2011):

$$[3.4] - [4.6] >= 0.8\,\mathtt{mag}$$

and

$$[4.6] - [12] > 2.2\mathtt{mag}$$
$$\&[4.6] - [12] < 4.2\mathtt{mag}$$
$$\&[3.4] - [4.6] > (0.1\mathtt{x}[4.6 - 12] + 0.38)\mathtt{mag}$$
$$\&[3.4] - [4.6] < 1.7\mathtt{mag}.$$

Here, we additionally add another 28 GPs that were detected in the four *WISE* bands with S/N > 3. The additional sample consists of 20 star-forming GPs and 8 AGN, or narrow-line Seyfert 1 galaxies (NLS1), GPs, the details of which (i.e., R.A., and decl.) are available in Cardamone et al. (2009). J0749 +3337 and J0822+2241 satisfy both of the AGN criteria within uncertainty. All of the optically identified AGN GPs can be classified as AGNs, and a large fraction of the star-forming GPs fall also within the criteria. However, Hainline et al. (2016) suggested that the selections do not guarantee the presence of an AGN, particularly for low-stellar-mass, high SFR, or high sSFR ($\log(\mathrm{sSFR/Gyr^{-1}}) > 0.1$) galaxies. Indeed, our GPs have high sSFRs (Figure 1).[10]

MIR SEDs have often been used to identify AGNs by detecting a power-law component originating in AGN-heated dust (e.g., Polletta et al. 2007). Spectral indices of luminous AGNs are typically $\alpha \gtrsim 0.5$ in the form of $S_\nu \propto \nu^{-\alpha}$ (Alonso-Herrero et al. 2006; Mullaney et al. 2011). The spectral indices of J0749+3337 and J0822+2241 derived from single power-law fits to *W1*, *W2*, and *W4* band photometry were $\alpha = 2.46 \pm 0.30$ and 2.02 ± 0.21, respectively. These are therefore supportive of the presence of an AGN. The *W3* band was excluded because various emission (e.g., polycyclic aromatic hydrocarbon (PAH) emission at the 7.7, 8.6, 11.3, and 12.7 μm bands) and absorption features (e.g., silicate absorption at 9.7 μm) contribute to emission. Note that we can obtain spectral indices consistent with those above even if we incorporate the *W3* emission into the fits.

We further investigate the origin of the MIR emission by focusing on the rest-frame 22 μm luminosities, which are 6.2 $\pm$ 0.5 $\times$ 10^{44} erg s^{-1} and 5.4 $\times$ 10^{44} erg s^{-1} for J0749+3337 and J0822+2241, respectively. The luminosities were derived based on the *W4* 22-μm band magnitudes of 6.8 and 6.4 in Vega for J0749+3337 and J0822+2241 and *K*-correction with $\alpha = 2$. In discussing whether star formation (SF) is the only MIR source, we make a comparison with the expected SF luminosity. The *W4* band is indeed suited for this purpose because dust may cause emission at the shorter wavelengths (*W1* and *W2*) to become extinct, and also because a correlation between the *W3* luminosity and SFR likely depends on the metallicity (Lee et al. 2013), making the comparison more complex. Lee et al. (2013) derived a correlation between the *W4* band and Hα luminosities, proxies of the SFR, as $\log(L_{\mathrm{H}\alpha}/\mathrm{erg\,s^{-1}}) = 0.49 + 0.96\log(L_{W4}/\mathrm{erg\,s^{-1}})$ with an intrinsic scatter of 0.21 dex. Their sample was composed of *WISE* 22 μm detected star-forming galaxies at $0.01 < z < 0.3$ in an SDSS catalog. The Hα luminosities, metallicities, and stellar masses of our GPs are within the ranges considered in Lee et al. (2013). If all of the band *W4* emission is ascribed to SF, $\log(L_{\mathrm{H}\alpha}/\mathrm{erg\,s^{-1}}) = 43.50 \pm 0.21$ and 43.43 ± 0.21 are

---

[10] By following Hainline et al. (2016), SFRs were calculated with Hα luminosity as $\log(\mathrm{SFR}/M_\odot\,\mathrm{yr^{-1}}) = \log(L_{\mathrm{H}\alpha}/\mathrm{erg\,s^{-1}}) - 41.27$.
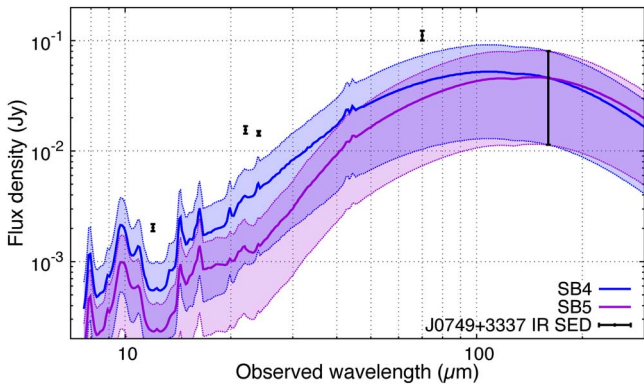
Figure 2. IR SED of J0749+3337 constructed from the *WISE* and *Spitzer*/MIPS data (black). Star-forming galaxy SEDs (SB4 and SB5 in Mullaney et al. 2011), normalized at the 160 μm flux density, are represented by blue and magenta lines. The shades indicate regions enclosed by the model SEDs normalized at the 1σ upper and lower 160 μm flux densities.

predicted. These are significantly larger by ≈0.6–0.8 dex than those observed (42.87 ± 0.02 of J0749+3337 and 42.67 ± 0.05 of J0822+2241). Thus, there may be an additional contribution by AGNs. Conservative 22 μm AGN luminosities, from which the SF contribution expected by the Hα emission is subtracted, are $4.8 \pm 0.9 \times 10^{44}$ erg s^{-1} and $4.5 \pm 0.6 \times 10^{44}$ erg s^{-1} for J0749+3337 and J0822+2241, respectively. The AGN MIR luminosities can be converted into hard X-ray 14–150 keV luminosities of $\log(L_{14-150\,\mathrm{keV}}/\mathrm{erg\,s}^{-1}) = 44.70 \pm 0.48$ and 44.67 ± 0.47 with 1σ scatters through the second equation in Table 3 of Ichikawa et al. (2017).[11] The correlation was derived based on *Swift*/BAT hard X-ray-selected nearby ($z < 0.3$) AGNs. Conventional 2–10 keV luminosities can be derived as $\log(L_{2-10\,\mathrm{keV}}/\mathrm{erg\,s}^{-1}) = 44.29$ and 44.26, respectively, by assuming a cut-off power law with $\Gamma = 1.7$ and $E_{\mathrm{cut}} = 360$ keV.

For J0749+3337 alone, we supplementarily examine the MIR luminosity expected from the far-infrared (FIR) luminosity that traces the SFR. J0822+2241 is not discussed here because no FIR data were available. We make a comparison between observed and model IR SEDs (Figure 2). FIR (70 μm and 160 μm) and additional MIR 24 μm photometry data from the *Spitzer*/MIPS is taken from Laag et al. (2010). The model SEDs are taken from Mullaney et al. (2011), who created five IR (6–1090 μm) templates by grouping 14 local (<80 Mpc) star-forming galaxies in terms of their overall shape and the relative strength of their PAH features. Out of the five IR templates, we adopt two (SB4 and SB5 in Mullaney et al. 2011) that considered galaxies with IR (8–1000 μm) luminosities of $\approx 10^{11.5} L_\odot$, comparable to that of J0749+3337 ($\sim 10^{11.7} L_\odot$; Laag et al. 2010). Figure 2 indicates MIR excess with respect to the models even in the most extreme case compatible with the observed 160 μm flux densities. This is consistent with the above statement.

3. *NuSTAR* Hard X-Ray Data Analysis

To obtain direct evidence for the presence of AGNs, we observed J0749+3337 and J0822+2241 by *NuSTAR*, which carries two independent focal plane modules (FPMA and FPMB), with on-source exposures of ≈ 19 ks and ≈ 22 ks,

respectively. Following the "*NuSTAR* Analysis Quickstart Guide,"[12] we used the standard `nupipeline` script for reprocessing. Our targets were very faint (<10^{-3} counts s^{-1}), and periods of high background (such as paths through or near the South Atlantic Anomaly (SAA)) must be excluded. Typical background rates observed with *NuSTAR* are ≲1 count s^{-1} integrated over the focal plane (Forster et al. 2014). Times of high background can be identified by simultaneously increased count rates in the detectors and shields that surround the focal planes. Using the telemetry reports made by the *NuSTAR* team, we checked the total event rates during all orbital passages of our observations. During the J0749+3337 observation, the event rate slightly increased around the standard SAA area (∼2 counts s^{-1}). In addition, high count rates occasionally occurred in the so-called tentacle region (Forster et al. 2014) near the SAA. Thus, we ran `nupipeline` to reject times with high count rates by setting options `saamode=optimized` and `tentacle=yes`. Background rates during the J0822+2241 observation were stable and low, and thus we adopted `saamode=none` and `tentacle=no`.

We defined source regions as 30″-radius circles centered at each optical position by taking account of the FWHM of the *NuSTAR* point-spread function (PSF; ≈18″). The size is much larger than the typical size of GPs (<1″; Cardamone et al. 2009). Background regions were off-source circular regions with a 30″-radius on the same detector. Then, we produced source and background spectra, and response files using the `nuproducts` task. The products of FPMA and FPMB were combined to provide better statistics by using the `addas-caspec` command. The systematic uncertainty between the two modules is likely much smaller than the statistical uncertainty. Figure 3 shows the obtained spectra, as well as the background contribution. This clearly illustrates that we detected no significant emission from J0749+3337 and J0822+2241 even in the most sensitive 8–24 keV band. Count rate upper limits at 3σ in the energy range are 5.7×10^{-4} counts s^{-1} and 4.5×10^{-4} counts s^{-1}, respectively. They are converted into 2–10 keV luminosities of $\approx 2 \times 10^{43}$ erg s^{-1} and $\approx 1 \times 10^{43}$ erg s^{-1}, respectively, by adopting a power-law model with $\Gamma = 1.7$. In Section 5.2, we further investigate how large absorbing column densities are needed to be consistent with the nondetection if there are AGNs with $\log(L_{2-10\,\mathrm{keV}}/\mathrm{erg\,s}^{-1}) \approx 44.3$ (Section 2).

## 4. *XMM-Newton* Soft X-Ray Data Analysis

The *XMM-Newton* data for J0749+3337 and J0822+2241 were obtained through the European Photon Imaging Camera/MOS (1 and 2) and PN detectors with a duration time of ≈44 ks and ≈34 ks. All observations were performed by adopting the Prime Full Window mode and the thin filter.

We reduced the data following the *XMM-Newton* ABC guide.[13] The raw PN and MOS data were reprocessed using pipelines of `epchain` and `emchain`, respectively. To filter periods with a high background, we created PN background light curves in the 10–12 keV band with `PATTERN=0` (single events), and those of the MOS in energies above 10 keV with the same pattern selection. Regarding the J0822+2241 data, we adopted background count rate thresholds of 0.35 s^{-1} and

---

[11] Although the energy band represented in Ichikawa et al. (2017) is 14–195 keV, the correct one is 14–150 keV.

[12] http://www.srl.caltech.edu/NuSTAR_Public/NuSTAROperationSite/SAA_Filtering/SAA_Filter.php
[13] https://heasarc.gsfc.nasa.gov/docs/xmm/abc/
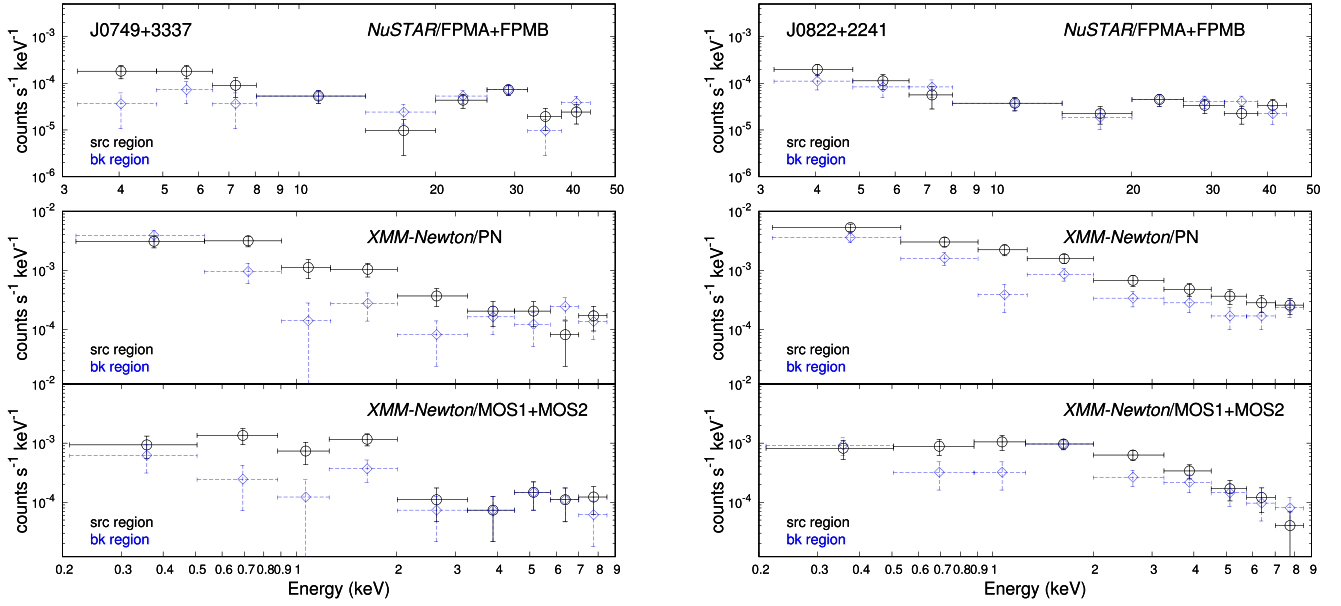
Figure 3. *NuSTAR* 3–50 keV and *XMM-Newton* 0.2–9 keV spectra taken from the source (black crosses with circles) and background (blue dashed crosses with diamonds) regions. The figures suggest that the GPs are detected in the soft band, but not in the hard band.

0.40 counts s^{-1} for the MOS and PN cameras, respectively. These are the recommended values in the guide. In contrast, we found two high-background flares during the J0749+3337 observation, and could not clearly remove the tails of the flares with the recommended thresholds. Thus, we excluded the first 10 ks and the last 11 ks to obtain clean data. The PN data were further limited to those with PATTERN $\leqslant$ 4 (single and double events) and FLAG = 0, corresponding to the most conservative screening criteria. For the MOS data selection, PATTERN $\leqslant$ 12 (single, double, triple, and quadruple events) was adopted. Central circular regions with 20″ and 25″ radii, larger than the FWHM of the *XMM-Newton* PSF ($\approx$6″), were set to extract J0749+3337 and J0822+2241 source events, respectively. The larger region was adopted for J0822+2241 because its X-ray image seemed to be slightly extended, although this was likely due to low photon statistic fluctuation. Each background spectrum was extracted from an off-source circular region with the same radius as that used for the source events. The spectra from the MOS1 and MOS2 detectors were combined into one. We analyzed the spectra in the 0.4–7.0 keV band, where J0749+3337 and J0822+2241 were significantly detected with S/N=(5.5, 4.1) and (6.6, 3.9) for (PN, MOS), respectively. The response files were generated in a standard manner for a point source.

4.1. XMM-Newton *Spectral Analyses*

We simultaneously fit the PN and MOS spectra (Figure 4) to increase the S/N. The spectra are binned so that each energy bin had at least one count. We thus determine best-fit models based on the *C*-statistic (Cash 1979), appropriate for low photon counts. Goodness of fit is examined by following the procedure given in Kaastra (2017), where the expected *C*-statistic value (C_{exp}) and variance ($\sigma_{C_{\mathrm{exp}}}$) from a model is compared with the observed value (C_{obs}). Note that the best-fit models found in the following sections are consistent with the nondetection by *NuSTAR*.

Essentially, we determine the best-fit models using the following model,

constant * TBabs * zTBabs * zpowerlw(Model1),

expressed in XSPEC terminology. The main component is the single absorbed power law (zTBabs*zpowerlw), and is adopted for a consistent comparison with the work by Brorby et al. (2016; Section 5.1). They parameterized the X-ray emission of low-mass galaxies by single power-law fits and discussed its association with SF. The power-law component may be ascribed to emission from high-mass X-ray binaries (HMXBs) and an AGN, if present. We also include the Galactic absorption, whose hydrogen column density is estimated from the nh command in HEASoft (Kalberla et al. 2005), with TBabs. We fix $N_{\mathrm{H}}^{\mathrm{Gal}} = 4.65 \times 10^{20}$ cm^{-2} and $N_{\mathrm{H}}^{\mathrm{Gal}} = 4.13 \times 10^{20}$ cm^{-2} for J0749+3337 and J0822+2241, respectively. To absorb systematic uncertainty in the normalization between the PN and MOS spectra, we apply the constant model, whose value is represented by $C_{\mathrm{MOS/PN}}$. To avoid implausible values, we allow it to vary only within 10%, a canonical range (e.g., see Figures 6 and 7 of Madsen et al. 2017). We finally obtain four free parameters: the photon index (Γ) and normalization of zpowerlw, the absorbing column density (N_{H}), and the cross-normalization between the spectra ($C_{\mathrm{MOS/PN}}$). Errors in intrinsic luminosity from the power law are constrained by replacing zpowerlw with pegpwrlw, which explicitly provides flux (or luminosity) errors in a given energy range.

We also apply another model that additionally takes into account emission from the hot interstellar medium (ISM) and young stellar objects (YSOs) according to the Mineo et al. (2012):

constant * TBabs * zTBabs(zpowerlw
+apec + zbremss)
(Model2).
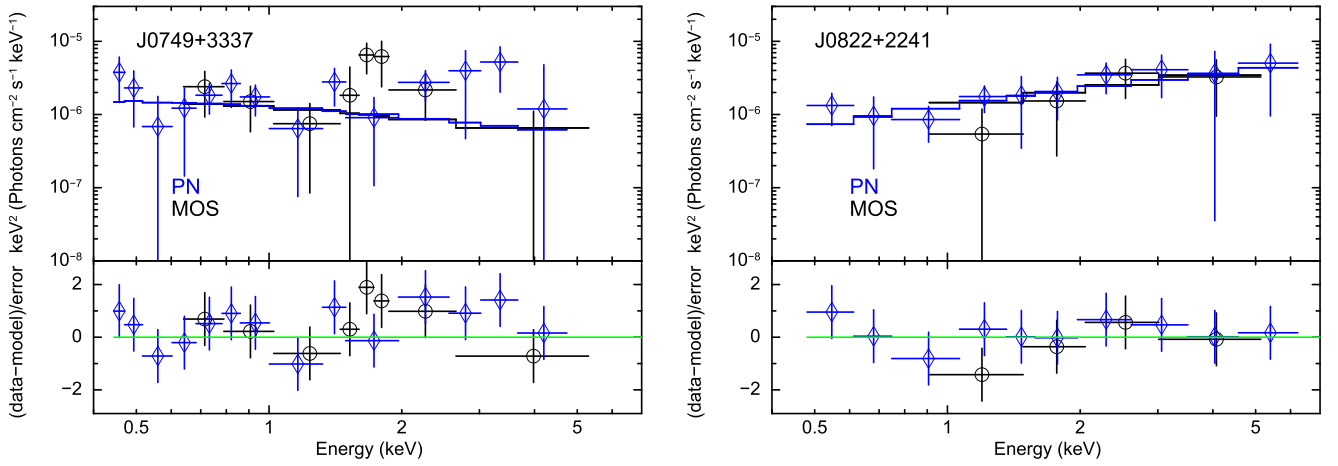
Figure 4. *XMM-Newton* 0.4–7.0 keV spectra, corrected for the response functions. Black crosses with circles and blue crosses with diamonds represent the MOS and PN spectra, respectively. For clarity, the spectra are rebinned with larger bin sizes. Each solid line is the best-fit, unabsorbed power-law model (Model1 in Table 3). Residuals are plotted in the lower panels.

Table 3
XMM-Newton Spectral Analysis Results

(1)	SDSS Name		J0749+3337		J0822+2241	
(2)	Model		Model1	Model2	Model1	Model2
(3)	$N_{\rm H}^{\rm Gal}$	$(10^{20}\ {\rm cm}^{-2})$	4.65		4.13	
(4)	$C_{\rm MOS/PN}$		$0.97^{+0.13}_{-0.07}$	$0.96^{+0.14}_{-0.06}$	$0.98^{+0.12}_{-0.08}$	$0.98^{+0.12}_{-0.08}$
(5)	$N_{\rm H}$	$(10^{22}\ {\rm cm}^{-2})$	$0.00(<0.45)$	$0.00(<0.47)$	$0.00(<0.35)$	$0.00(<0.38)$
(6)	Γ		$2.6^{+1.0}_{-0.8}$	$2.5^{+1.1}_{-0.9}$	$1.3^{+0.8}_{-0.4}$	$1.3^{+0.8}_{-0.5}$
(7)	Norm	$(10^{-6}\ {\rm photon\ cm}^{-2}\ {\rm s}^{-1}\ {\rm keV}^{-1})$	$2.6^{+1.0}_{-0.9}$	$2.3^{+1.0}_{-0.9}$	$1.9^{+1.8}_{-0.6}$	$1.8^{+1.8}_{-1.0}$
(8)	$F_{0.5-2\,{\rm keV}}$	$(10^{-15}\ {\rm erg\ cm}^{-2}\ {\rm s}^{-1})$	2.8	2.8	3.1	3.1
(9)	$F_{0.5-8\,{\rm keV}}$	$(10^{-15}\ {\rm erg\ cm}^{-2}\ {\rm s}^{-1})$	4.2	4.4	11	11
(10)	$F_{2-10\,{\rm keV}}$	$(10^{-15}\ {\rm erg\ cm}^{-2}\ {\rm s}^{-1})$	1.6	1.8	10	10
(11)	$L_{0.5-2\,{\rm keV}}$	$(10^{41}\ {\rm erg\ s}^{-1})$	$8.5^{+5.5}_{-3.8}$	$7.6^{+3.7}_{-3.0}$	$4.0^{+5.5}_{-1.7}$	$3.9^{+3.5}_{-1.6}$
(12)	$L_{0.5-8\,{\rm keV}}$	$(10^{41}\ {\rm erg\ s}^{-1})$	12^{+9}_{-5}	12^{+6}_{-5}	14 ± 7	14 ± 5
(13)	$L_{2-10\,{\rm keV}}$	$(10^{41}\ {\rm erg\ s}^{-1})$	$4.2^{+10.7}_{-3.5}$	$4.5^{+8.1}_{-3.4}$	13 ± 9	13 ± 7
(14)	$C_{\rm obs}/C_{\rm exp}$ /d.o.f		$92/87 \pm 10/109$	$92/88 \pm 11/109$	$200/210 \pm 15/241$	$200/210 \pm 15/241$
(15)	S/N (PN, MOS)		5.5, 4.1		6.6, 3.9	

Note. Columns: (1) SDSS source name. (2) Model1 is the absorbed power law, and Model2 consists of the absorbed power law, the optically thin thermal emission, and bremsstrahlung. The latter two thermal emission are fixed. (3) Hydrogen column density of the Galactic absorption. (4) Ratio between the MOS and PN spectral models. (5) Hydrogen column density of extragalactic absorption. (6) Power-law photon index. (7) Power-law normalization at 1 keV. (8)–(10) Observed fluxes in the 0.5–2, 0.5–8, and 2–10 keV bands. (11)–(13) Absorption-corrected intrinsic luminosities in the 0.5–2, 0.5–8, and 2–10 keV bands. (14) Observed C-statistic value, and expected C-statistic value with its 1σ uncertainty, and degrees of freedom. (15) S/N in the 0.4–7.0 keV band. (The fluxes and luminosities are estimated from the PN spectra.)

The ISM emission is modeled by optically thin thermal emission (apec) with a temperature of 0.24 keV, the average value of those measured in nearby galaxies. The metal abundance is set to 0.40 for J0749+3337 and 0.25 for J0822+2241 according to each oxygen abundance ratio. The YSO emission is modeled by bremsstrahlung (zbremss) with a canonical temperature of 3 keV (Winston et al. 2007; Mineo et al. 2012). Luminosities from the ISM and YSOs are expected to increase with SFR as $L_{0.5-2\,{\rm keV,ISM}}/{\rm SFR} = 5.2 \times 10^{38}$ (erg s$^{-1}/M_{\odot}$ yr^{-1}) and $L_{2-10\,{\rm keV,YSO}}/{\rm SFR} = 1.7 \times 10^{38}$ (erg s$^{-1}/M_{\odot}$ yr^{-1}). Accordingly, we fix the normalizations of the two thermal emission at those corresponding to the expected luminosities. Note that we do not consider X-ray emission from low-mass X-ray binaries, cataclysmic variables, or active binaries. Given correlations of their

luminosities and stellar mass (Gilfanov 2004; Bogdán & Gilfanov 2011), at most $L_{\rm X} \sim 10^{38}$ erg s^{-1} is expected from those populations. This is much smaller than observed luminosities ($\sim 10^{41}$ erg s^{-1}). Finally, we obtain the same four free parameters as in Model1. We stress that because the two models provide similar values (Table 3), our discussion does not depend on the adopted models, as detailed below.

4.1.1. Soft X-Ray Band J0749+3337 Spectra

Fitting Model1, we obtain an unabsorbed ($N_{\rm H} < 4.5 \times 10^{21}$ cm^{-2}), soft ($\Gamma = 2.6^{+1.0}_{-0.8}$) power-law model in $C_{\rm obs}/C_{\rm exp} = 92/87 \pm 10$. The rest-frame 0.5–8 keV intrinsic luminosity ($L_{0.5-8\,{\rm keV}}$) is measured to be $1.2^{+0.9}_{-0.5} \times 10^{42}$ erg s^{-1}. Model2

also provides a similar result, where $N_H < 4.7 \times 10^{21}$ cm^{-2}, $\Gamma = 2.5^{+1.1}_{-0.}$, and $L_{0.5-8\,keV} = 1.2^{+0.6}_{-0.5} \times 10^{42}$ erg s^{-1}.

4.1.2. Soft X-Ray Band J0822+2241 Spectra

Similarly to the J0749+3337 case, Model1 can reproduce the J0822+2241 spectra well with insignificant absorption ($N_H < 3.5 \times 10^{21}$ cm^{-2}) and a harder photon index ($\Gamma = 1.3^{+0.8}_{-0.4}$) in $C_{obs}/C_{exp} = 200/210 \pm 15$. The luminosity is $L_{0.5-8\,keV} = 1.4 \pm 0.7 \times 10^{42}$ erg s^{-1}. A similar result can be obtained by fitting Model2 (Table 3).

5. Discussion

5.1. Origin of Soft X-Ray Emission

We investigate the origin of the soft X-ray emission reported in Section 4.1 in terms of the luminosity. To discuss whether or not SF can reproduce $\approx 10^{42}$ erg s^{-1}, we refer to Brorby et al. (2016). They derived a correlation between the X-ray (0.5–8 keV) luminosity, SFR, and oxygen abundance ratio ($12 + \log(O/H)$) for Lyman break analogs: supercompact, UV-luminous galaxies at $z < 0.3$, regarded as nearby analogs of more distant Lyman break galaxies such as GPs. The SFR used in the correlation is defined as the sum of dust-obscured and unobscured SFRs (Brorby & Kaaret 2017; see also Hirashita et al. 2003). The dust unobscured SFRs of $59 \pm 3\,M_\odot$ yr^{-1} for J0749+3337 and $37 \pm 4\,M_\odot$ yr^{-1} for J0749+3337 derived by Cardamone et al. (2009) may therefore be underestimated. Thus, by dividing the unobscured Hα-based SFRs with an absorbed Lyman continuum fraction of 0.48 ± 0.20 (Hirashita et al. 2003), we estimate the total SFRs to be $123 \pm 51\,M_\odot$ yr^{-1} and $78 \pm 34\,M_\odot$ yr^{-1} for J0749+3337 and J0822+2241, respectively. Regarding the stellar mass and oxygen abundance ratio, we adopt those from Izotov et al. (2011). The two values were derived, respectively, based on SED fits and the so-called direct method, which uses the electron temperature within the [O III] zone from the [O III]$\lambda 4363/(\lambda 4959 + \lambda 5007)$ line ratio. Then, predicted 0.5–8 keV luminosities from the correlation are $\log(L^{SF}_{0.5-8\,keV}/\mathrm{erg\,s^{-1}}) = 41.81 \pm 0.38$ (1σ) for J0749+3337 and $\log(L^{SF}_{0.5-8\,keV}/\mathrm{erg\,s^{-1}}) = 41.74 \pm 0.39$ (1σ) for J0822+2241. These are consistent with the observed 0.5–8 keV luminosities of $\log(L_{0.5-8\,keV}/\mathrm{erg\,s^{-1}}) = 42.08^{+0.33}_{-0.18}$ for J0749+3337 and 42.15 ± 0.22 for J0822+2241. Thus, the soft X-ray emission can be ascribed solely to SF, or likely HMXBs. Therefore, we cannot detect any evidence for soft X-ray emission from AGNs.

5.2. NuSTAR Nondetection due to Heavy Obscuration?

The 22 μm luminosities of our sample would seem to originate from AGN emission, and their expected luminosities would be $\log(L_X/\mathrm{erg\,s^{-1}}) \sim 44$ (see Section 2). However, *NuSTAR* does not show any significant detection from those sources. This seemingly contradictory result could be naturally described if the central engine is heavily obscured. Mainly utilizing the *NuSTAR* 8–24 keV data, we compute how large absorbing hydrogen column densities are required to be consistent with the nondetection.

We construct our model by adopting a Monte-Carlo-based numerical AGN torus model[14] e-torus. The original version was created by Ikeda et al. (2009) and has often been used to

---

study AGN tori (e.g., Kawamuro et al. 2013, 2016b; Ricci et al. 2013, 2014; Tazaki et al. 2013; Guainazzi et al. 2016; Tanimoto et al. 2016, 2018; Oda et al. 2018; Yamada et al. 2018). The e-torus model calculates reflected spectra from constant-density cold matter that has two cone-shaped holes along the polar axis (see Figure 2 of Ikeda et al. 2009). The ratio of the inner and outer radii is fixed at 0.01. The solar metal abundance is adopted. The torus property is determined by the hydrogen column density in the equatorial plane (N^{eq}_H), and the half opening (θ_{op}) and inclination (θ_{inc}) angles. These angles are defined so that 0° and 90° correspond to the pole direction and the equatorial direction, respectively. The GPs are optically nonactive galaxies, implying that a torus with a small opening angle prevents formation of the narrow line region (i.e., Ueda et al. 2007). Thus, within the acceptable range of $\theta_{op} = 10°$–70°, we adopt $\theta_{op} = 10°$, corresponding to a covering factor of 98%, while θ_{inc} is set to 60° as a representative value to ensure an obscured AGN. The primary X-ray emission is modeled by a cut-off power-law spectrum with a high-energy cutoff of 360 keV and $\Gamma = 1.7$ (e.g., Kawamuro et al. 2016a). Adopting alternative values (i.e., $\Gamma = 1.9$, $\theta_{inc} = 89°$, and $\theta_{op} = 37°$) instead of the default values, we can confirm that our conclusion is little affected. Specifically, our model is represented as

```
torusabs * zpowerlw * zhighect
  +zpowerlw * zhighect
  *mtable{e − torus_20161121_2500M.fits}
  +atable{refl_fe_torus.fits}
  +[Best − fit Model of the XMM − Newton Spectra],
```

almost the same as those used in past studies (e.g., Oda et al. 2018; Tanimoto et al. 2018). From the first to the third terms, we take account of the absorbed cut-off power-law component from an AGN, the reflected emission, and the accompanying 6.4 keV iron–Kα line. The fourth term means that we include emission expected from each best-fit model (Model1) determined in the *XMM-Newton* spectra (Section 4.1).

We estimate power-law normalizations that reproduce the 3σ source count rates for various column densities in the equatorial plane (N^{eq}_H), and compute corresponding intrinsic X-ray luminosities. The result is plotted in Figure 5 and is compared with the 14–150 keV (plus 2–10 keV) luminosities expected from the 22 μm ones to constrain acceptable ranges of N^{eq}_H. A point of concern is that when the column density is lower than a certain value, the torus models tend to exceed the *XMM-Newton* spectra while being consistent with the *NuSTAR* observations. Therein, we take account of the maximum luminosity accepted by the *XMM-Newton* spectra and also plot the results. Specifically, we fit a suite of torus models having a given column density with various normalizations together with an absorbed power-law model to the *XMM-Newton* spectra. Then, we compute C_{obs}, C_{exp}, and $\sigma_{C_{exp}}$ following Kaastra (2017). Finally, we search for a maximum normalization where $C_{obs} = C_{exp} + 2.78 \times \sigma_{C_{exp}}$, equivalent to 3$\sigma$, and plot the corresponding luminosity. Eventually, Figure 5 indicates that the column density (N^{eq}_H) must be larger than 2×10^{24} cm^{-2} for J0749+3337 and 5×10^{24} cm^{-2} for J0822+2241. Thus, if present, their AGNs should be heavily obscured.

The low metal abundances of the GPs make photoelectric absorption more ineffective compared with solar absorption. In this case, higher column densities are needed. As a simple
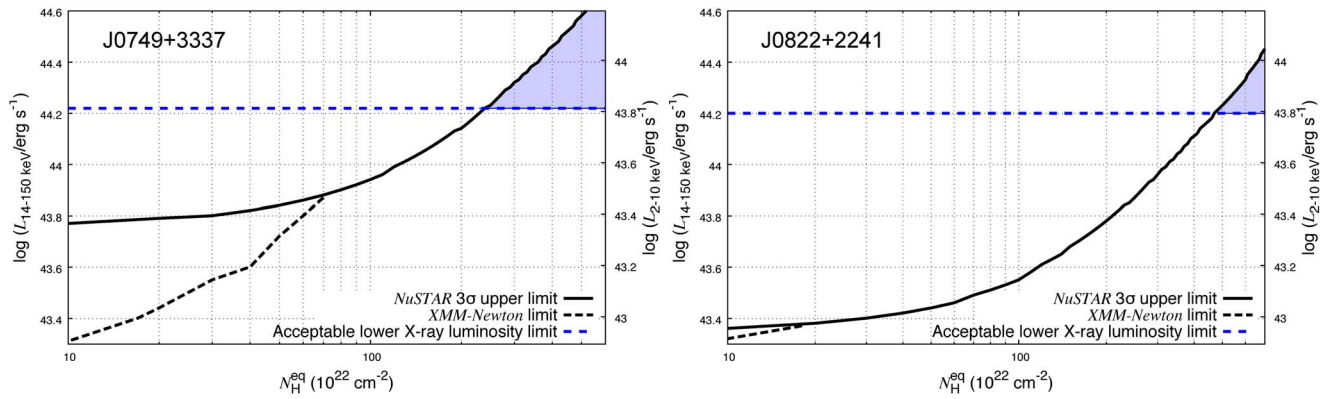
Figure 5. Expected X-ray luminosity vs. hydrogen column density in the equatorial plane. The right $L_{2-10\,\mathrm{keV}}$-axis is scaled with the left $L_{14-150\,\mathrm{keV}}$-axis under a cut-off power-law model with $\Gamma = 1.7$ and $E_{\mathrm{cut}} = 360$ keV. The blue dashed line represents the lower X-ray luminosity limit expected from the observed 22 μm luminosity for each source. The maximum luminosities accepted by the *XMM-Newton* spectra for a given column density are denoted by black dashed lines. In other words, luminosities above the limits erroneously exceed the *XMM-Newton* spectra. Blue shades correspond to acceptable areas and indicate lower limits of $N_{\mathrm{H}}^{\mathrm{eq}} \gtrsim 2 \times 10^{24}$ cm^{-2} and $N_{\mathrm{H}}^{\mathrm{eq}} \gtrsim 5 \times 10^{24}$ cm^{-2} for J0749+3337 and J0822+2241.

estimate, by considering that the column density is inversely proportional to the metal abundance for a given level of absorption, $N_{\mathrm{H}}^{\mathrm{eq}} \gtrsim 5 \times 10^{24}$ cm^{-2} for J0749+3337 and $N_{\mathrm{H}}^{\mathrm{eq}} \gtrsim 2 \times 10^{25}$ cm^{-2} for J0822+2241 are expected. The estimate may be reasonable but unrigorous for various reasons; for example, the reflection component seen around 30 keV and the Compton scattering are not taken into consideration in this discussion.

5.3. MIR Emission due to SF?

We also discuss another possibility for a non-AGN case for our GPs. In this case, the red MIR colors and steep spectral slopes may be ascribed to YSOs. Note that the asymptotic giant branch (AGB) star is another stellar MIR emitter, but is not likely to be the main source given that the *W3-W4* colors of our GPs (3.6 and 2.9 for J0749+3337 and J0822+2241) are redder than expected from usual AGBs ($\lesssim 2$; Koenig & Leisawitz 2014; Lian et al. 2014). It has been suggested that very young YSOs in particular, with an age $\lesssim$ a few Myr show NIR and MIR emission from optically thick disks (e.g., Lada 1987; Strom et al. 1989; Haisch et al. 2001; Dunham et al. 2014). Motivated by this fact, some studies proposed selection and classification criteria for YSOs that use the *WISE* data (e.g., Koenig & Leisawitz 2014; Kang et al. 2017). The results indicate that Class I and II YSOs have MIR colors similar to those observed in luminous AGNs; that is, in our GPs as well. Moreover, an MIR index defined as $d\log(\lambda S_\lambda)/d\log\lambda$ has often been used for the classification of conventional YSO classes. (Greene & Lada 1996; Majaess 2013; Marton et al. 2013; Kang et al. 2017). Characterizing the MIR slopes of our GPs based on Marton et al. (2013), we find that they show $d\log(\lambda S_\lambda)/d\log\lambda \approx 1$, consistent with those of Class I YSOs. Thus, if SF is the main source that powers the MIR emission, the Class I YSO is a plausible type of star that mainly contributes to it. This YSO interpretation is consistent with the idea that GPs correspond to an early phase of galaxy formation.

6. Summary

To discuss whether or not the two GPs (J0749+3337 and J0822+2241) host AGNs, suggested from the MIR *WISE* observations, we obtained the initial hard X-ray (>10 keV) data using *NuSTAR*. Then, including the *XMM-Newton* data

(<10 keV), we explored X-ray evidence for the presence of an AGN. Our results are summarized as follows.

1. Both GPs were detected in all *WISE* bands, and have red colors, steep spectral indices of $\alpha \sim 2$, and higher MIR luminosities ($\approx$5–6 $\times 10^{44}$ erg s^{-1}) than expected from the Hα emission. These data are consistent with the presence of an AGN.

2. We detected no significant hard X-ray (8–24 keV) emission from the GPs.

3. Soft (0.4–7 keV) X-ray emission was significantly (>3σ) detected. The 0.5–8 keV luminosities reach $\approx 10^{42}$ erg s^{-1}, and can be explained by SF only.

4. Considering the AGN X-ray luminosities expected from the MIR data, we estimated the minimum column densities required to be consistent with the nondetection by *NuSTAR*. The result indicated that if present, the AGNs in J0749+3337 and J0822+2241 were obscured with column densities $N_{\mathrm{H}}^{\mathrm{eq}} \gtrsim 2 \times 10^{24}$ cm^{-2} and $N_{\mathrm{H}}^{\mathrm{eq}} \gtrsim 5 \times 10^{24}$ cm^{-2}, respectively. If smaller abundances were assumed, larger column densities of $N_{\mathrm{H}}^{\mathrm{eq}} \gtrsim 5 \times 10^{24}$ cm^{-2} for J0749+3337 and $N_{\mathrm{H}}^{\mathrm{eq}} \gtrsim 2 \times 10^{25}$ cm^{-2} for J0822+2241 were expected.

5. Finally, the possibility remains that no AGN exists and is not the main source that powers the MIR emission. In this case, young Class I YSOs would be plausible main contributors in the MIR band (Section 5.3). This is consistent with a previous study (Section 1) where low-mass galaxies with active SF, such as GPs, probably in an early phase of galaxy growth, were suggested to reproduce photometric MIR properties similar to those of AGN hosts. If true, this implies that diagnostics that use MIR photometry data alone may misidentify such galaxies as AGNs.

To finally distinguish between the two possibilities, MIR spectroscopy may be an option. Detection of a deep silicate absorption feature at 9.7 μm may favor the presence of an AGN deeply embedded in the dust (e.g., Dudley & Wynn-Williams 1997; Evans et al. 2003), because it is difficult to produce if sources are largely distributed, as in SF. Also, equivalent widths of PAH emission may be examined given that a lower (higher) value is expected if an AGN (SB) dominates the MIR emission (e.g., Imanishi et al. 2007;

Veilleux et al. 2009). In the future, the *JWST*/MIRI spectroscopy observation with high sensitivity will be a promising way to draw a strong conclusion.

ORCID iDs

Taiki Kawamuro ⓘ https://orcid.org/0000-0002-6808-2052
Yoshihiro Ueda ⓘ https://orcid.org/0000-0001-7821-6715
Kohei Ichikawa ⓘ https://orcid.org/0000-0002-4377-903X
Masatoshi Imanishi ⓘ https://orcid.org/0000-0001-6186-8792
Takuma Izumi ⓘ https://orcid.org/0000-0001-9452-0813
Atsushi Tanimoto ⓘ https://orcid.org/0000-0002-0114-5581
Kenta Matsuoka ⓘ https://orcid.org/0000-0002-2689-4634

References

Alonso-Herrero, A., Pérez-González, P. G., Alexander, D. M., et al. 2006, ApJ, 640, 167
Arnaud, K. A. 1996, adass V, 101, 17
Baldassare, V. F., Reines, A. E., Gallo, E., & Greene, J. E. 2015, ApJL, 809, L14
Basu-Zych, A. R., Lehmer, B. D., Hornschemeier, A. E., et al. 2013, ApJ, 774, 152
Begelman, M. C., Volonteri, M., & Rees, M. J. 2006, MNRAS, 370, 289
Bogdán, Á., & Gilfanov, M. 2011, MNRAS, 418, 1901
Bromm, V., & Yoshida, N. 2011, ARA&A, 49, 373
Brorby, M., & Kaaret, P. 2017, MNRAS, 470, 606
Brorby, M., Kaaret, P., Prestwich, A., & Mirabel, I. F. 2016, MNRAS, 457, 4081
Cardamone, C., Schawinski, K., Sarzi, M., et al. 2009, MNRAS, 399, 1191
Cash, W. 1979, ApJ, 228, 939
Chakraborti, S., Yadav, N., Cardamone, C., & Ray, A. 2012, ApJL, 746, L6
Chen, C.-T. J., Brandt, W. N., Reines, A. E., et al. 2017, ApJ, 837, 48
Dudley, C. C., & Wynn-Williams, C. G. 1997, ApJ, 488, 720
Dunham, M. M., Stutz, A. M., Allen, L. E., et al. 2014, in Protostars and Planets VI, ed. H. Beuther et al. (Tucson, AZ: Univ. Arizona Press), 195
Evans, A. S., Becklin, E. E., Scoville, N. Z., et al. 2003, AJ, 125, 2341
Forster, K., Harrison, F. A., Dodd, S. R., et al. 2014, Proc. SPIE, 9149, 91490R
Fragos, T., Lehmer, B., Tremmel, M., et al. 2013, ApJ, 764, 41
Gandhi, P., Yamada, S., Ricci, C., et al. 2015, MNRAS, 449, 1845
Gebhardt, K., Bender, R., Bower, G., et al. 2000, ApJL, 539, L13
Gilfanov, M. 2004, MNRAS, 349, 146
Greene, J. E. 2012, NatCo, 3, 1304
Greene, T. P., & Lada, C. J. 1996, AJ, 112, 2184
Guainazzi, M., Risaliti, G., Awaki, H., et al. 2016, MNRAS, 460, 1954
Gültekin, K., Cackett, E. M., Miller, J. M., et al. 2009, ApJ, 706, 404
Gürkan, M. A., Freitag, M., & Rasio, F. A. 2004, ApJ, 604, 632
Haehnelt, M. G., & Rees, M. J. 1993, MNRAS, 263, 168
Hainline, K. N., Reines, A. E., Greene, J. E., & Stern, D. 2016, ApJ, 832, 119
Haisch, K. E., Jr., Lada, E. A., Piña, R. K., Telesco, C. M., & Lada, C. J. 2001, AJ, 121, 1512

Harrison, F. A., Craig, W. W., Christensen, F. E., et al. 2013, ApJ, 770, 103
Hasinger, G., Miyaji, T., & Schmidt, M. 2005, A&A, 441, 417
Henry, A., Scarlata, C., Martin, C. L., & Erb, D. 2015, ApJ, 809, 19
Hirashita, H., Buat, V., & Inoue, A. K. 2003, A&A, 410, 83
Ichikawa, K., Imanishi, M., Ueda, Y., et al. 2014, ApJ, 794, 139
Ichikawa, K., Ricci, C., Ueda, Y., et al. 2017, ApJ, 835, 74
Ikeda, S., Awaki, H., & Terashima, Y. 2009, ApJ, 692, 608
Imanishi, M., Dudley, C. C., Maiolino, R., et al. 2007, ApJS, 171, 72
Imanishi, M., Dudley, C. C., & Maloney, P. R. 2001, ApJL, 558, L93
Imanishi, M., Dudley, C. C., & Maloney, P. R. 2006, ApJ, 637, 114
Imanishi, M., Nakagawa, T., Ohyama, Y., et al. 2008, PASJ, 60, S489
Imanishi, M., Nakagawa, T., Shirahata, M., Ohyama, Y., & Onaka, T. 2010, ApJ, 721, 1233
Izotov, Y. I., Guseva, N. G., & Thuan, T. X. 2011, ApJ, 728, 161
Jansen, F., Lumb, D., Altieri, B., et al. 2001, A&A, 365, L1
Jarrett, T. H., Cohen, M., Masci, F., et al. 2011, ApJ, 735, 112
Jaskot, A. E., & Oey, M. S. 2013, ApJ, 766, 91
Kaastra, J. S. 2017, A&A, 605, A51
Kalberla, P. M. W., Burton, W. B., Hartmann, D., et al. 2005, A&A, 440, 775
Kang, S.-J., Kerton, C. R., Choi, M., & Kang, M. 2017, ApJ, 845, 21
Kauffmann, G., Heckman, T. M., Tremonti, C., et al. 2003, MNRAS, 346, 1055
Kawamuro, T., Ueda, Y., Tazaki, F., Ricci, C., & Terashima, Y. 2016a, ApJS, 225, 14
Kawamuro, T., Ueda, Y., Tazaki, F., & Terashima, Y. 2013, ApJ, 770, 157
Kawamuro, T., Ueda, Y., Tazaki, F., Terashima, Y., & Mushotzky, R. 2016b, ApJ, 831, 37
Kewley, L. J., Dopita, M. A., Sutherland, R. S., Heisler, C. A., & Trevena, J. 2001, ApJ, 556, 121
Koenig, X. P., & Leisawitz, D. T. 2014, ApJ, 791, 131
Kormendy, J., & Ho, L. C. 2013, ARA&A, 51, 511
Kormendy, J., & Richstone, D. 1995, ARA&A, 33, 581
Laag, E., Croft, S., Canalizo, G., et al. 2010, AJ, 140, 2052
Lada, C. J. 1987, in Proc. IAU Symp. 115, Star-forming Regions, ed. M. Piembert & J. Jugaku (Dordrecht: Reidel), 1
Lee, J. C., Hwang, H. S., & Ko, J. 2013, ApJ, 774, 62
Lian, J., Zhu, Q., Kong, X., & He, J. 2014, A&A, 564, A84
Linden, T., Kalogera, V., Sepinsky, J. F., et al. 2010, ApJ, 725, 1984
Lintott, C. J., Schawinski, K., Slosar, A., et al. 2008, MNRAS, 389, 1179
Lodato, G., & Natarajan, P. 2006, MNRAS, 371, 1813
Madsen, K. K., Beardmore, A. P., Forster, K., et al. 2017, AJ, 153, 2
Magorrian, J., Tremaine, S., Richstone, D., et al. 1998, AJ, 115, 2285
Mainzer, A., Grav, T., Bauer, J., et al. 2011, ApJ, 743, 156
Majaess, D. 2013, Ap&SS, 344, 175
Marconi, A., & Hunt, L. K. 2003, ApJL, 589, L21
Marconi, A., Risaliti, G., Gilli, R., et al. 2004, MNRAS, 351, 169
Marton, G., Verebélyi, E., Kiss, C., et al. 2013, AN, 334, 924
Mateos, S., Alonso-Herrero, A., Carrera, F. J., et al. 2012, MNRAS, 426, 3271
Mezcua, M., Civano, F., Fabbiano, G., Miyaji, T., & Marchesi, S. 2016, ApJ, 817, 20
Mezcua, M., Civano, F., Marchesi, S., et al. 2018, MNRAS, 478, 2576
Mineo, S., Gilfanov, M., & Sunyaev, R. 2012, MNRAS, 426, 1870
Mullaney, J. R., Alexander, D. M., Goulding, A. D., & Hickox, R. C. 2011, MNRAS, 414, 1082
Nguyen, D. D., Seth, A. C., den Brok, M., et al. 2017, ApJ, 836, 237
Nguyen, D. D., Seth, A. C., Neumayer, N., et al. 2018, ApJ, 858, 118
Oda, S., Ueda, Y., Tanimoto, A., & Ricci, C. 2018, ApJ, 855, 79
Polletta, M., Tajer, M., Maraschi, L., et al. 2007, ApJ, 663, 81
Reines, A. E., & Comastri, A. 2016, PASA, 33, e054
Ricci, C., Paltani, S., Awaki, H., et al. 2013, A&A, 553, A29
Ricci, C., Ueda, Y., Paltani, S., et al. 2014, MNRAS, 441, 3622
Sartori, L. F., Schawinski, K., Treister, E., et al. 2015, MNRAS, 454, 3722
Satyapal, S., Secrest, N. J., McAlpine, W., et al. 2014, ApJ, 784, 113
Secrest, N. J., Satyapal, S., Gliozzi, M., et al. 2015, ApJ, 798, 38
Shankar, F., Salucci, P., Granato, G. L., De Zotti, G., & Danese, L. 2004, MNRAS, 354, 1020
Stern, D., Assef, R. J., Benford, D. J., et al. 2012, ApJ, 753, 30
Strom, K. M., Newton, G., Strom, S. E., et al. 1989, ApJS, 71, 183
Svoboda, J., Douna, V., Ehle, M., & Orlitová, I. 2018, arXiv:1810.09318
Tanimoto, A., Ueda, Y., Kawamuro, T., et al. 2018, ApJ, 853, 146
Tanimoto, A., Ueda, Y., Kawamuro, T., & Ricci, C. 2016, PASJ, 68, S26
Tazaki, F., Ueda, Y., Terashima, Y., Mushotzky, R. F., & Tombesi, F. 2013, ApJ, 772, 38
Thornton, C. E., Barth, A. J., Ho, L. C., Rutledge, R. E., & Greene, J. E. 2008, ApJ, 686, 892

Ueda, Y., Akiyama, M., Hasinger, G., Miyaji, T., & Watson, M. G. 2014, ApJ, 786, 104

Ueda, Y., Akiyama, M., Ohta, K., & Miyaji, T. 2003, ApJ, 598, 886

Ueda, Y., Eguchi, S., Terashima, Y., et al. 2007, ApJL, 664, L79

Ueda, Y., Hashimoto, Y., Ichikawa, K., et al. 2015, ApJ, 815, 1

Veilleux, S., Rupke, D. S. N., Kim, D.-C., et al. 2009, ApJS, 182, 628

Volonteri, M. 2010, A&ARv, 18, 279

Volonteri, M., Lodato, G., & Natarajan, P. 2008, MNRAS, 383, 1079

Wilms, J., Allen, A., & McCray, R. 2000, ApJ, 542, 914

Winston, E., Megeath, S. T., Wolk, S. J., et al. 2007, ApJ, 669, 493

Wright, E. L., Eisenhardt, P. R. M., Mainzer, A. K., et al. 2010, AJ, 140, 1868

Yamada, S., Ueda, Y., Oda, S., et al. 2018, ApJ, 858, 106

Yang, H., Malhotra, S., Gronke, M., et al. 2016, ApJ, 820, 130